A&A 466, 339–346 (2007)
DOI: 10.1051/0004-6361:20065129

Astronomy & Astrophysics

Birth and evolution of a dense coronal loop in a complex flare region

L. Bone[1], J. C. Brown[1], L. Fletcher[1], A. Veronig[2], and S. White[3]

[1] Astrophysics Group, Department of Physics and Astronomy, University of Glasgow, Glasgow, G12 8QQ, UK
e-mail: laura@astro.gla.ac.uk
[2] Institute for Geophysics, Astrophysics and Meteorology, University of Graz, Universitätsplatz 5, 8010 Graz, Austria
[3] University of Maryland, Astronomy Department, College Park, MD 20742, USA

Received 2 March 2006 / Accepted 10 October 2006

ABSTRACT

Context. During the 14th/15th of April 2002, several flares occurred in NOAA active region complex 9893/9910. Two of these were previously interpreted as having anomalously high coronal column densities.
Aims. We develop a scenario using multiwavelength observations to explain the high coronal column density ($\approx 10^{20}$ cm^{-2}) present at the onset of the 14th April 2002 M3.7 hard X-ray event.
Methods. Prior to this event a series of flares occurred in close temporal and spatial proximity. We observe the sequence of flares in a multiwavelength regime from radio to hard X-rays. This allows us to study the particle acceleration and plasma evaporation in these events.
Results. The observations of these flares lead us to propose a sequence of reconnections between multiple systems of loops in a 3 dimensional field geometry. We suggest that the dense loops in the M3.7 event can be explained as being already filled with plasma from the earlier events; these loops then themselves become unstable or reconnect leading to particle acceleration into an overdense coronal environment. We explore the possibility that a high-beta disruption is behind the instability of these dense loops, leading to the 14th April 2002 M3.7 event and the observation of hard X-rays in the corona at energies up to ≈50 keV.

Key words. Sun: activity – Sun: flares – Sun: radio radiation – Sun: X-rays, gamma rays

1. Introduction

Coronal hard X-ray sources in solar flares have the potential to reveal much about ambient conditions in the corona as well as the flare acceleration process. While coronal radio sources produced by flares are relatively common and easy to detect through their gyrosynchrotron radiation as nonthermal electrons spiral along magnetic fields (e.g., Takakura et al. 1985), detecting hard X-rays from the same electrons in the corona, in contrast to the X-rays they produce when they strike the chromosphere, is a much more difficult proposition. Since the ambient density in the corona is usually much smaller than in the chromosphere, bremsstrahlung there is less effective and footpoint hard X-ray sources tend to be much brighter than their coronal counterparts. If the hard X-ray observations have limited dynamic range, the coronal sources can be hard to detect. Thus the presence of coronal hard X-ray (HXR) sources was first inferred in occulted events (flares having their HXR footpoints behind the solar limb) during the 1970's (Frost & Dennis 1971; Hudson 1978) using data from HXR spectrometers on the OSO 5 and OSO 7 satellites. Multispacecraft observations of occulted solar flares were later used to infer altitudes of coronal sources of >25 000 km (Kane et al. 1979). In the earliest imaging observations, with SMM/HXIS, van Beek et al. (1981) found coronal emission at between 3.5−16 keV extending up to 30 000 km above the solar limb. Observations of an occulted flare (i.e. with footpoints beyond the solar limb) with the Solar X-ray Telescope on Hinotori extended the energy range at which such sources were known to be present up to at least 25 keV (Takakura et al. 1983). At this time, coronal HXR sources were generally interpreted as thermal bremsstrahlung from hot coronal plasma, significant non thermal thick target emission being expected only at the footpoints (Brown & McClymont 1976).

The launch of the *Yohkoh* satellite led to several further reports of coronal hard X-ray emission. The claim of an impulsive, and by implication, non-thermal coronal component was first made by Masuda et al. (1994) using *Yohkoh*/HXT. The source was present at energies up to at least 53 keV, but the observation is limited by dynamic range and source confusion issues encountered when imaging the usually diffuse coronal HXR sources in the presence of intense chromospheric ones. In a study of 14 occulted *Yohkoh*/HXT flares, Tomczak (2001) put the observations of non-thermal coronal sources on a stronger footing, demonstrating that coronal sources exhibit both gradual and impulsive HXR emission apparently originating in the same source, with the impulsive spikes being more energetic and having harder spectral indices.

Since its launch in 2002, the Ramaty High Energy Solar Spectroscopic Imager (RHESSI) has observed a number of coronal hard X-ray sources (Sui & Holman 2003; Sui et al. 2004; Veronig & Brown 2004; Kane et al. 2005), both moving (Liu et al. 2004; Veronig et al. 2006) and stationary. The frequency and diversity of these sources and the development of the physics therein has been one of the major achievements of RHESSI. There are many theoretical interpretations of such sources, including (i) locations of a fast-mode shock, occurring where the outflow jet from a coronal reconnection region impacts on a dense and static loop system below (Tsuneta & Naito 1998);

(ii) signatures of the current sheet itself or its heated outflow regions (Sui & Holman 2003); (iii) large pitch angle particles trapped and possibly further accelerated in the field below a reconnecting coronal structure (Somov & Kosugi 1997; Fletcher & Martens 1998) at normal coronal densities; (iv) thick-target bremsstrahlung emission from non-thermal particles in a dense part of the corona (Wheatland & Melrose 1995; Veronig & Brown 2004; Lin et al. 2003); and (v) super-hot coronal plasma (Lin et al. 1981; Kosugi et al. 1994; Krucker et al. 2003). Theoretically, the simplest explanation is an enhanced coronal density, but we must then offer an explanation as to why the density, and the emission measure are large. It is of course possible that different models are appropriate for different flares or different phases of the flare.

In this paper we concentrate on an event in which the RHESSI emission up to ≈50 keV is believed to be due to coronal thick-target bremsstrahlung. The M3.7 flare on the 14th of April 2002 – which was not occulted – showed RHESSI HXR emission primarily from the corona, with little or no footpoint emission during most of the flare. Veronig & Brown (2004) interpreted this as being caused by high coronal column densities, consistent with a non-thermal coronal thick-target. At the onset of this event the column density derived from GOES soft X-ray data was already rather high ($\approx 10^{20}$ cm^{-2}), suggesting that the loop was already filled with plasma, possibly from early-phase evaporation before the onset of the flare impulsive phase. Such observations are not without precedent; Kosugi et al. (1994) also interpreted the appearance of a coronal HXR source in the second part of the impulsive phase as suggestive of high density in the flare loop.

For the 14-April-2002 M3.7 flare, complementary multi-wavelength observations provide information that allows us to explore further the birth and evolution of the dense coronal loop. We use HXR, radio, EUV and magnetogram data in the phase prior to the "dense loop" flare in an attempt to understand the AR configuration and the circumstances under which a flare could happen in a loop already having a high density. In the following section we present the observational material, in Sect. 4 our interpretation of the events and in Sect. 5 some discussion and conclusions.

2. Observations

Data from the RHESSI satellite, which allows high resolution imaging and spectroscopy from 3 keV to 17 MeV, and from the Nobeyama radioheliograph, which images at 17 and 34 GHz provide complementary information on the acceleration of high energy electrons in this active region, with a similar spatial and temporal resolution. We also use data from the Nobeyama radio polarimeters, which measure total flux in 1, 2, 3.75, 9.74, 17, 34 and 80 GHz, bands to determine radio spectra for this event (no data were available for the 80 GHz band).

The GOES soft X-ray light-curve, with three flare events marked, is shown in Fig. 1. The 14-April-2002 M3.7 event occurred in NOAA active region 9893, at approximately N19 W60. This active region was part of a complex, with an older decaying region (9893), visible in the top left frame of Fig. 2 nearby a more recently emerged active region (9901). The sequence of MDI images in Fig. 2 shows how the two active regions evolve in the days before the flares. Note in particular that the positive polarity of 9901 overlaps in longitude with the negative polarity of 9893.

A C7.2 flare (flare 1) occurred in AR 9893 at 22:30 accompanied by a jet in EIT and a type III burst. A second small

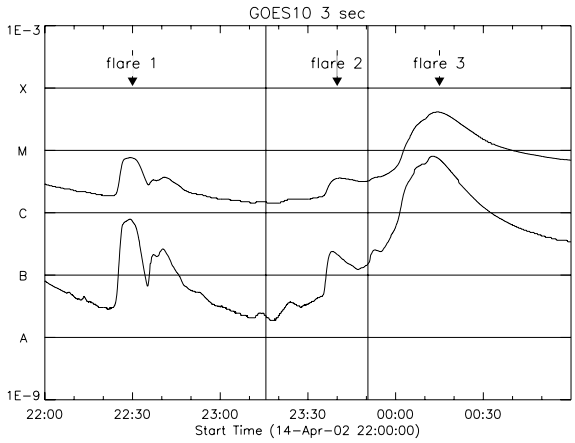

Fig. 1. GOES plot showing the three flares that occurred in AR9893 on the 14th April. The top curve is the 1−8 Å band, the bottom is the higher energy 0.5−4 Å band. Between the two vertical lines RHESSI was in eclipse.

flare, or possibly a pre-flare event (flare 2) occurred at approximately 23:33, during which time RHESSI was in eclipse, as shown in Fig. 1. The M3.7 flare (flare 3), analysed in Veronig & Brown (2004), began shortly after RHESSI came out of eclipse at approximately 23:54. Both flare 1 and flare 2 occur in nearby loops in AR 9893.

Flare 2 peaked around 23:34, at which time we see a compact loop brightening in EIT and an increase in the GOES soft X-ray flux (Fig. 1). RHESSI is in night, however the Nobeyama radio heliograph data are available and show a strong, polarised eastern footpoint source and a weaker, polarised western footpoint source as well as unpolarised coronal emission in the 17 GHz band (Fig. 3).

The polarised footpoint source is consistent with gyrosynchrotron emission from non-thermal electrons at this footpoint, probably with a steep spectrum since there is no detectable emission in 34 GHz imaging at this time (but the 34 GHz emission is quite strong in flare 3, see below). The 17 GHz coronal source is only visible between 23:33:30 and 23:35:20, but this is probably a dynamic range effect, due to the increasing brightness of the footpoint source. The microwave footpoint source remains consistently bright throughout flares 2 and 3 and is co-spatial in the earlier and later images (at approximately $x = 790''$, $y = 370''$). Data from EIT show that flares 2 and 3 take place in different, although nearby, loop systems.

The loop system in which flare 3 occurs, nearby to that in which flare 2 occurs, began to brighten in 17 GHz radio, as early as 23:33, just after the impulsive phase of flare 2. RHESSI is in eclipse so there is no hard X-ray data at this time. The loop can also be seen brightening in EIT from this time, although it is clearest from 23:48, consistent with the 12 min cadence of the instrument. In the 17 GHz radio images initially only the southern footpoint brightens, and later the entire loop brightens around the onset of HXR emission (Fig. 3).

The lightcurves at 17 and 34 GHz and HXR 25−50 keV, as well as the thermal emission seen in soft X-rays, are shown in Fig. 4. The similarity of the rapidly fluctuating parts of the radio and HXR 25−50 keV lightcurves suggests that the electrons producing both kinds of emission belong to the same nonthermal population. In addition, the radio light curves show a strong thermal component, particularly noticeable during the decay phase of the lightcurve, that matches the shape predicted from the temperature and emission measure of hot plasma seen in the GOES

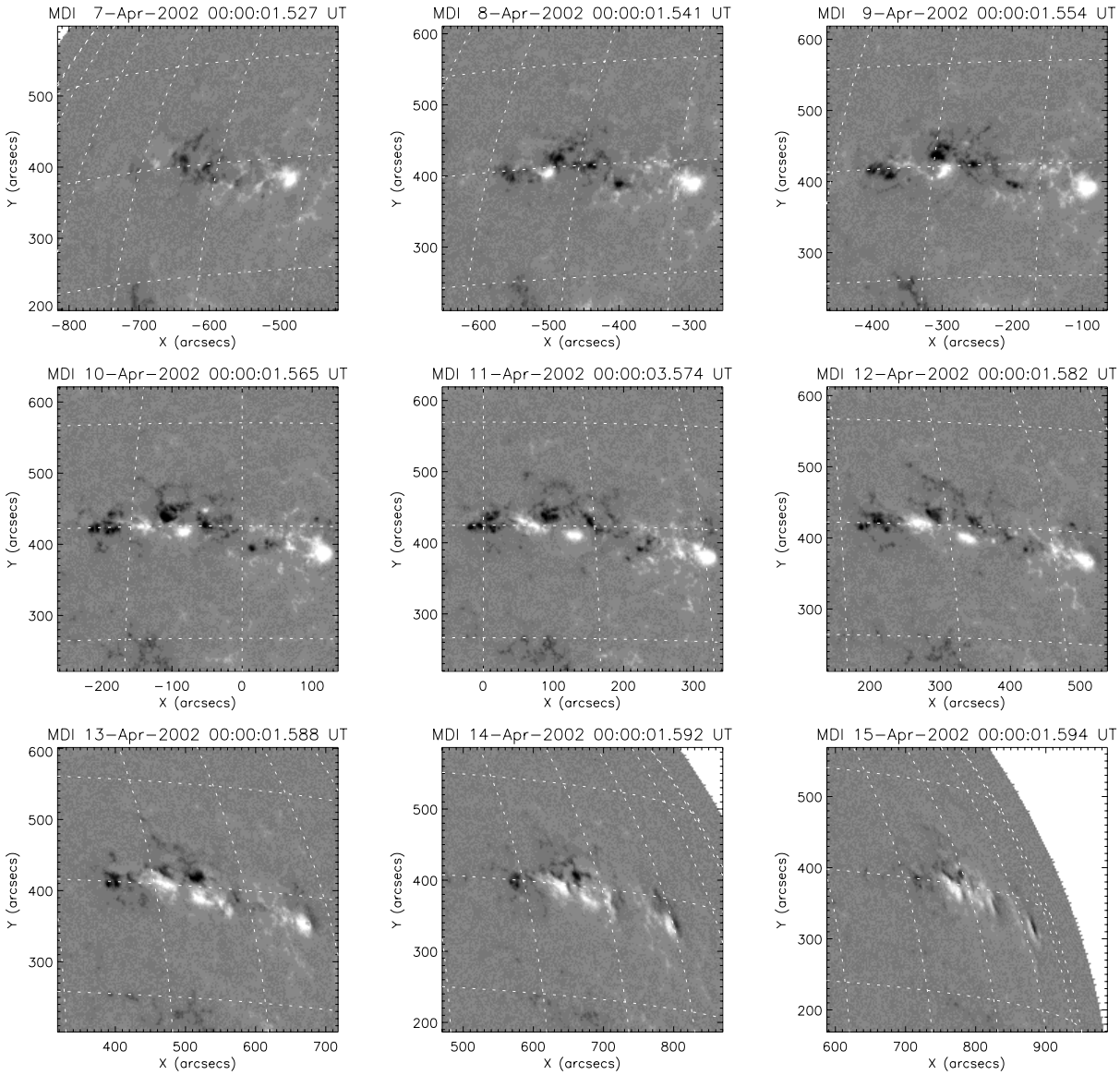

Fig. 2. The evolution of the magnetic field in the active region complex between 7-April-2002 and 15-April-2002, showing the development of complexity at the interface between the two regions. Positive polarity is indicated by white, negative by black. The easternmost region is AR9901 and the region closest to the western limb is AR9893.

soft X-ray data. (The fact that the GOES data underpredict the level of thermal radio emission by a factor of order 2 can be attributed to the presence of cooler material which contributes relatively more to the radio flux via bremsstrahlung.) Although there is almost no detectable emission in hard X-rays above 50 keV, gyrosychrotron emission from nonthermal electrons is clearly present in the rapidly fluctuating short-lived peaks in the radio light curves. Since an observable gyrosynchrotron radio flux can be obtained with a smaller number of electrons than an observable bremsstrahlung HXR flux, there is no inconsistency in only seeing evidence for the higher-energy accelerated electrons in the radio data.

At the peak of flare 3 (around 00:10) we see a sharp spike in both the radio and HXR emission. A strongly polarised source also appears at a remote point in the 17 GHz Stokes V radio emission from 00:09:58–00:11:08. This source demonstrates a similar level of polarisation (10%) as the main flaring source. This remote source coincides with the location of the western footpoint of flare 2 at (825″, 366″) as seen in EIT, some distance from the flare 3 loop. This western footpoint source is only seen briefly in radio and HXR at this time (Fig. 3), during which we also note a distinct hardening of the spectral index in the HXR spectrum (the radio spectrum also appears to harden, but this is complicated by the relatively large contribution of thermal bremsstrahlung at 34 GHz). Figure 5 is a summary plot, showing the relationship of the radio footpoints and RHESSI sources to the photospheric magnetic fields and coronal structures. Notice that – within the accuracy of the co-alignments ($\approx 2''$) the main microwave sources and the RHESSI loop appear at the interface between the two active regions, with one RHESSI footpoint in the negative field of AR9893, and the other in the positive field of AR9901. This suggests that flare 2 resulted in the formation of a loop connecting the two regions. The western footpoint radio source occurs in the positive field of AR9893. Spectral information about the radio emission can be obtained from the Nobeyama radio polarimeters. During the flare readings were made every 0.1 s, to increase signal to noise the data were integrated over 300 points (30 s), the preflare background

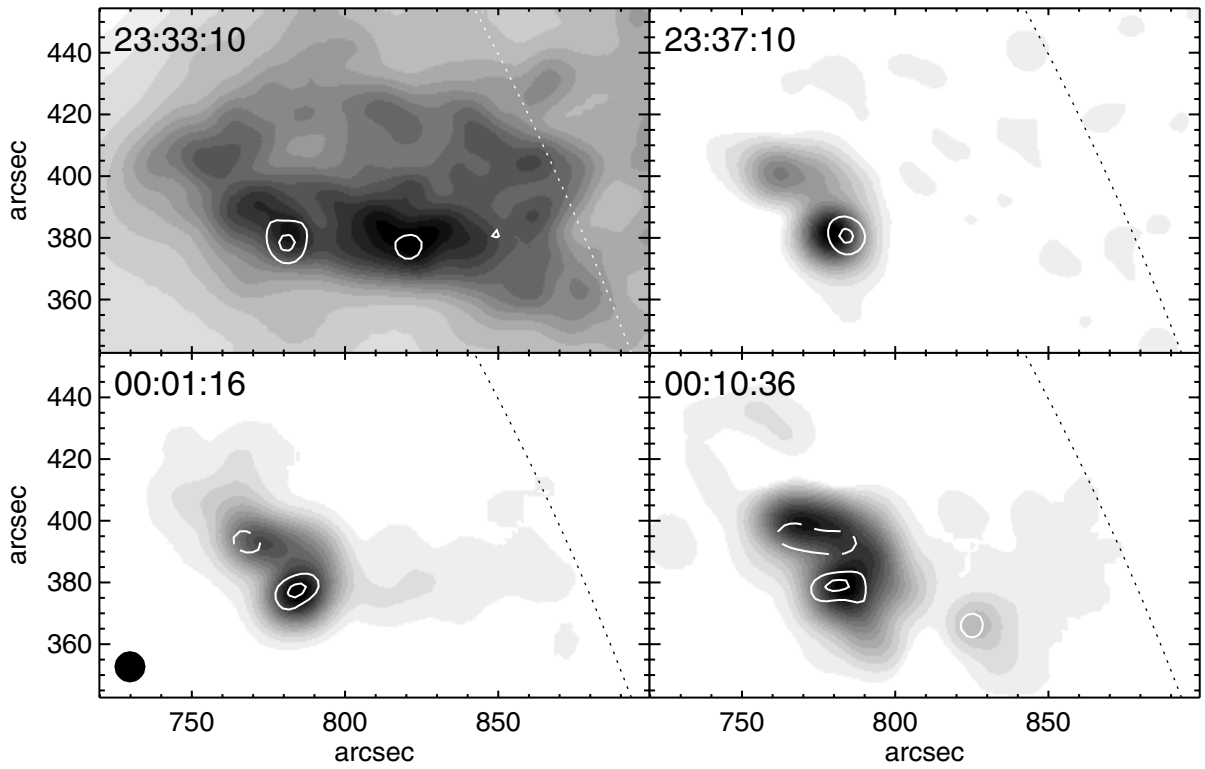

Fig. 3. The evolution of microwave emission over the flare, in total intensity with polarisation overlayed with contours ≥50%. The first image shows the later half of flare 2, with one strong footpoint, one weak footpoint and diffuse coronal emission. The second image is between the flares still showing a strong footpoint source. The third image shows the whole loop in which flare 3 occurs beginning to brighten and the fourth image shows the whole loop at the peak of the flare, along with a remote polarised source consistent with the western footpoint source of flare 2. All polarised emission above 50% comes from the positive component. The beam size is shown by the circle in the lower left corner.

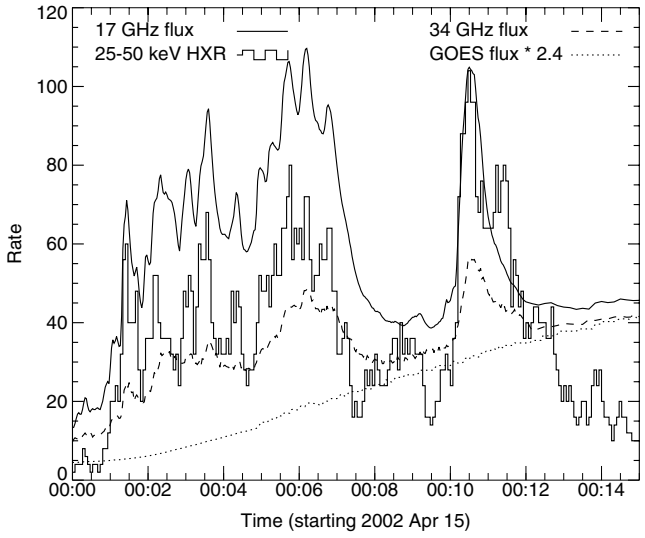

Fig. 4. Lightcurves of the radio and hard X-ray fluxes during the impulsive phase of flare 3. Four quantities are plotted: the 17 GHz flux in sfu (solid line), the 25−50 keV hard X-ray photon count rate scaled to fit on the plot (histogram), the 34 GHz flux (dashed line), and the radio flux from optically thin bremsstrahlung predicted from the GOES soft X-ray fluxes assuming coronal abundances, multiplied by 2.4 (dotted line). The rapidly-fluctuating components of the radio and hard X-ray lightcurves exhibit similar behaviour, including an initial impulsive phase, a decline in emission and then a strong impulsive spike and a rapid (<20 s) variation. In addition to the rapidly fluctuating component, the radio light curves show a steady component rising for most of the period shown that matches the shape of the GOES thermal bremsstrahlung prediction extremely well.

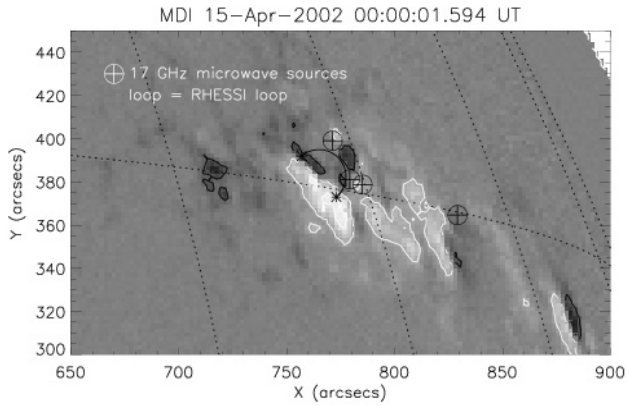

Fig. 5. 17 GHz radio footpoints and RHESSI loop overlaid on the magnetic field and coronal images. The HXR footpoints appear to occur one on either side of the interface between the two ARs, suggesting that flare 2 resulted in the formation of a loop connecting the two regions.

– which is averaged over an entire days data – subtracted and the data plotted. There was no visible emission in the 1 and 80 GHz bands, which leaves a limited number of points to obtain spectral information with, however the data can be fitted with a model spectrum which allows information about many parameters to be estimated.

Because the full formalism used to calculate gyrosychrotron emission is somewhat cumbersome, it is usual to use some sort of simplification when calculating parameters from gyrosychrotron emission. The most usual simplifications used are the numerical expressions of Dulk & Dennis (1982). However, these

Table 1. Parameters obtained from fitting model spectrum to NoRP data.

Time	Spectral index γ	$A(t) \times$ 1e30	B in Gauss	α
00:01:10	4.6	2.6	145	0.25
00:02:10	3.9	7.9	145	0.27
00:03:10	3.8	10.5	140	0.28
00:04:10	3.8	10.5	140	0.29
00:05:10	4.0	5.8	190	0.29
00:06:10	4.5	8.0	200	0.29
00:07:10	4.1	8.7	180	0.29
00:08:10	3.3	4.0	140	0.30
00:09:10	3.1	3.8	120	0.30
00:10:10	4.1	18.0	145	0.27

have a limited range of validity and the applicability breaks down for high harmonics and large viewing angles (θ with respect to B). Therefore, it is not necessarily the best approach for fitting spectra close to the limb.

The model spectra are therefore calculated using the computational method described in Ramaty et al. (1994). A thin target model for gyrosychrotron emission is assumed in which the instantaneous emission is proportional to the differential number density of relativistic electrons $N_e(E, t)$. A power law distribution in kinetic energy is assumed $N_e(E, t) = A(t)E^{-\gamma}$. The gyrosychrotron radiation is evaluated using the formalism given in Ramaty (1969) which requires the evaluation of a series of Bessel functions to calculate the emissivity.

The output model spectrum is dependent on; $A(t)$; γ; the magnetic field B; the angular size of the source and the viewing angle; the range of electron energies – although electrons with energies below about 100 keV contribute very little energetically to the gyrosychrotron emission and can in most cases be neglected; the transition energy to the full relativistic formalism – which can be taken to be about 3 MeV except in cases where the viewing angle is close to 0°, which is not the case here, and the Razin parameter. The Razin parameter is given by $\alpha = 1.5\nu_B/\nu_p$ where ν_B is the gyrofrequency and ν_p is the plasma frequency, it is a measure of how gyrosychrotron emission from an electron of Lorentz factor Γ is strongly suppressed at low frequencies if $\alpha\Gamma < 1$ and at all frequencies if $\alpha\Gamma \ll 1$.

The fits of the data to the model were made at 1 min intervals during the period of the M3.7 flare when the gyrosychrotron emission was most intense. The fits were made with a constant source size, taken to be 20″, and a constant viewing angle, taken to be 66°. The range of electron energies calculated over was 100 keV to 100 MeV. The best fit parameters are shown in Table 1.

We can see that the thin target spectral indices are slightly harder than those we would expect from the hard X-ray emission ranging from 3 to 4.6. This suggests a thick target spectral index of 5 to 6.6, slightly harder than seen in the HXR spectra. For significant numbers of gyrosynchrotron emitting electrons in excess of the 100 keV threshold to be obtained with a power law distribution, it is not surprising that the spectral index must be slightly harder.

3. Parameters derived from the observations

Certain parameters for the later two flares can be directly inferred from observations. The temperature and emission measure for each can be taken from GOES and for the second flare from RHESSI. The spectral index for the later flare can be estimated from RHESSI and radio. Although radio emission is visible for the earlier flare in the 17 GHz radio frequency band there is no data either from the radioheliograph or the polarimeters at higher frequencies, this prevents us from estimating a spectral index for this flare. From the spectral fits we can estimate the magnetic field strength in the second flare and the Razin parameter. We can also estimate loop lengths from RHESSI and radio data for the second flare and from radio for the initial flare.

Having determined the emission measures as well as the area, length and thus volume of the flaring loops, it is possible from there to determine an estimate for the column density in each flare, since emission measure $EM = n^2V$ and the column density $N = nL/2$. We can also estimate a density n from the radio emission in the second flare if we assume that the excess emission at 2 GHz is due to plasma emission. Since the plasma emission is related to the density by $\nu_p = 10^4\sqrt{n}$. This allows an independent estimate of the column density.

Hard X-ray spectra from RHESSI are used to calculate the beam power in erg/s using the formula in Brown (1971) at energies greater than E_0 for a low energy cut off E_0. In this case the low energy cutoff was set at 25 keV. The thick target beam injection rate in electrons/s is related to the power injected by

$$E_0F_0(t) = \frac{\delta(t) - 2}{\delta(t) - 1}P_0. \quad (1)$$

It was also possible to calculate the electron number directly from the radio emission since the total number of electrons in the loop $n(E) = AE^{-\gamma}$. This was only possible in the second flare where there was both RHESSI coverage and broad band radio emission.

The beam driven evaporation can be calculated using the beam power and area and spectral index from the RHESSI data by (modifying the treatment in Brown (1973) for closed loops cf. Kontar et al. 2003)

$$N_{\rm beam} \approx 8.2 \times 10^{19}\left[7.7 \times 10^{-12}B\left(\frac{\delta}{2}, \frac{1}{3}\right)(\delta - 2)\frac{P_{25}}{A}p\right]^{2/(\delta-2)} \quad (2)$$

where $p \leq 1$ corrects for finite loop-top pressure. Conductive evaporation near the event peak, in near hydrostatic equilibrium follows a scaling law such that (Rosner et al. 1978)

$$N_{\rm cond}({\rm cm}^{-3}) \approx 1.4 \times 10^{20}T_7^2. \quad (3)$$

$E_{\rm loop}$ defines the minimum energy that electrons would need to have to pass through a loop of a certain column density. Electrons below this energy are collisionally stopped. $E_{\rm loop} = (3KN)^{1/2} \approx 8.8N_{19}^{1/2}$ where $K = 2\pi e^4\Lambda$ is the Coulomb logarithm.

The estimates for these parameters are shown in Table 2. Certain parameters could only be defined for flare 3 where there is more complete multiwavelength coverage, however from GOES we can estimate a column density for flare 2 and a geometry for it from 17 GHz radio emission. This allows us to make estimates of the conductive evaporation and stopping energy.

4. Interpretation

To summarise the sequence of events leading to flare 3: prior to the onset of the flare 3 HXR impulsive phase (i.e. the M3.7 event), the loop which will become bright in HXR emission during flare 3, brightens gradually in both EIT 195 Å and 17 GHz radio emission. Combined with the already bright, polarised radio emission from the southern footpoint, this is evidence that fast electrons may already be present in the flare 3 loop, i.e. it

Table 2. Parameters inferred directly from observation of the two sequential flares in AR9893/9901 and parameters derived from the observations.

	Observational parameters			
	Flare 2			
	GOES M	GOES C	RHESSI	Radio
Peak temperature (MK)	7	10	–	–
Peak E Measure (10^{49} cm^{-3})	0.2	0.05	–	–
Peak photon spectral index (γ)	–	–	–	–
Magnetic field (Gauss)	–	–	–	–
Razin parameter (α)	–	–	–	–
Length (10^9 cm)	–	–	–	4.0
footpoint area (10^{17} cm^2)	–	–	–	2.5
	Flare 3			
Peak temperature (MK)	16	16	35	–
Peak E Measure (10^{49} cm^{-3})	5.0	2.0	3.5	–
Peak photon spectral index (γ)	–	–	5.9	5.1
Magnetic field (Gauss)	–	–	–	150
Razin parameter (α)	–	–	–	0.27
Length (10^9 cm)	–	–	4.5	2.9
footpoint area (10^{17} cm^2)	–	–	2.0	2.5
	Derived parameters			
	Flare 2			
Column density 10^{19} cm^{-2}	9.0	4.5	–	–
Electron Number (electrons/s)	–	–	–	–
Power (erg/s)	–	–	–	–
Beam evaporation 10^{19} cm^{-2}				
Conductive evaporation 10^{19} cm^{-2}	6.9	14.0	–	
Radiative losses (erg/s)	1×10^{26}	3×10^{25}	–	–
Conductive losses (erg/s)	2.2×10^{26}	7.9×10^{26}	–	–
Stopping energy (keV)	18.6	26.4	–	–
	Flare 3			
Column density 10^{19} cm^{-2}	35.0	22.0	9.3	5.0
Electron Number (electrons/s)	–	–	1.4×10^{36}	5.6×10^{34}
Power (erg/s)	–	–	7.0×10^{27}	–
Beam evaporation 10^{19} cm^{-2}	–	–	9.7	
Conductive evaporation 10^{19} cm^{-2}	36.0	36.0	170	–
Stopping energy (keV)	52.0	41.0	27.8	19.6

suggests that there is low-level continuous ongoing particle acceleration prior to the impulsive phase onset.

It can be seen from the GOES plots of density that at the onset of flare 3 there is already a reasonably high column density in the loop. At the peak of flare 2 the column density estimated from GOES is around 9×10^{19} cm^{-2}, this column density increases steadily until the onset of flare 3, when it rises rapidly, conductive evaporation allows for a significant amount of plasma to be evaporated into the loop at this point. In the radio emission we see that while we initially have one loop bright, within a few minutes the configuration of the magnetic field appears to have changed and the other loop is much brighter. This would suggest that through reconnection a certain amount of material and fast electrons are transferred onto the second loop. The fast electrons will lead to some evaporation from the footpoints, either through direct beam driven effects or through conductive evaporation.

There are several ways to explain the observation outside the "standard model". The electron acceleration in flare 3 might not be not directly related to magnetic reconnection. For example, the flare 3 magnetic instability could severely perturb the dense loop by a mechanical impulse or Alfvén wave, leading to local acceleration throughout the dense loop – perhaps by a stochastic process – but without changing its topology. Secondly – and this is the scenario we favour – the dense loop, which exists in a complicated magnetic environment, might itself become unstable, resulting in particle acceleration and further reconnection with other magnetic structures. In this context, in 4.1 we briefly investigate the high beta MHD instability proposed by Shibasaki (2001).

We propose that flare 2 takes place between AR 9901 and AR 9893 in the manner shown in the cartoon Fig. 6. A sequence of MDI images shows that the positive polarity of 9901 overlaps in longitude the negative polarity in 9893, leading to the configuration in frame (a). Reconnection between them would produce a short, sheared loop, onto which plasma evaporates. This dense loop becomes unstable – we propose this occurs via a high β plasma instability. The result of the instability is local particle acceleration in the dense loop, and – as the dense loop rises because of the high β instability – reconnection with the just-created overlying field.

How MHD instabilities accelerate electrons is a matter for debate. There is no universally accepted model for electron acceleration, however there are three frequently-discussed broad model classes. Firstly, if the instability develops a current sheet and reconnection, then the electrons may be accelerated in the reconnecting current sheet or X-point itself (e.g. Litvinenko 2003; Somov & Kosugi 1997; Hamilton et al. 2005). Secondly, the electrons might be accelerated in fast or slow shocks, possibly those produced in a reconnection outflow region (e.g. Ellison & Ramaty 1985; Tsuneta & Naito 1998). Thirdly, electrons might be (stochastically or systematically) accelerated in turbulent magnetic field within a loop, again possibly, but not necessarily, a post-reconnection loop (e.g. Miller et al. 1996; Karlický & Kosugi 2004). We suggest that the different spectral

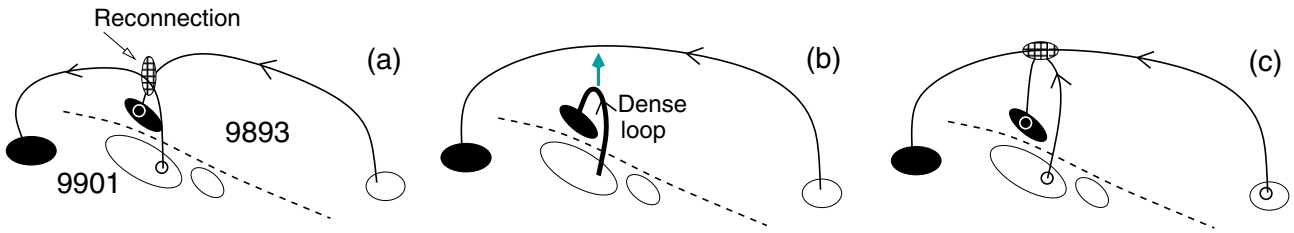

Fig. 6. Sketch of the magnetic reconfiguration occurring in flares 2 and 3. Flare 2 occurs at the interface between AR 9901 and AR 9893, and we suggest that it leads to the formation of a dense loop between the two active regions, plus overlying field connecting the other polarities of the two ARs. This small loop, observed to be dense and hot, is unstable to the ballooning instability, which leads to particle acceleration in the loop (see text) and also the rise of the loop until it interacts with the overlying field. At this point the western footpoint becomes visible briefly.

characteristics of the main impulsive phase and the later spike in flare 3, when the spectrum hardens, at the time when the reconnection in overlying field is taking place, indicate that more than one type of acceleration is occurring.

4.1. The high beta instability

For loops in which there is (relatively) low magnetic field, and a high density, Shibasaki (2001) discussed the possibility that the local mode of the interchange instability occurs – the "ballooning instability". This has been extensively studied in Tokamak fusion reactors (Park et al. 1995). The ballooning instability converts thermal and kinetic energy in the loop into turbulent wave energy, non-thermal particle energy and plasma bulk kinetic energy (plasma flows and ejection) (Shibasaki 2001).

The thermal plasma beta is

$$\beta_{\rm T} = \frac{P}{B^2/8\pi} \tag{4}$$

for coronal conditions $\beta_{\rm T}$ can be written in normalised units of the solar corona as

$$\beta_{\rm T} \sim \frac{N_9 T_6}{B_G^2} \simeq 0.1 \tag{5}$$

using the observationally-derived values for N, T from the X-ray emission and B from the radio emission.

If flows are not taken into account, then the ballooning instability occurs when;

$$\beta_{\rm T} \geq \beta_{\rm crit} = 2\frac{l_{\rm p}}{R}, \tag{6}$$

where $l_{\rm p}$ is the loop internal radius and R is the radius of curvature. Using $l_{\rm p} = 1.2 \times 10^8$ cm and $R = 2.5 \times 10^9$ cm from RHESSI images $\beta_{\rm crit} = 0.05$. We obtain values of $\beta_{\rm T}$ using the temperature from GOES Chianti measurements at the start of the flare and density derived from the emission measure. This gives a value for $\beta_{\rm T} = 0.06$, using the magnetic field obtained from spectral fits to the radio data at this time of 140 G. If we take the value of temperature and emission measures obtained from RHESSI spectral fits we get a $\beta_{\rm T}$ of $\approx$0.1 since the emission measure seen by RHESSI is smaller and thus the density is less but the temperature is significantly higher.

Throughout most of the RHESSI flare 3 observations, only the loop-top source is visible. The spike at 00:10 UT accompanied by a hardening of the HXR spectral index and the appearance of the third strongly polarised source and of an Hα remote brightening, both coincident with the western footpoint of flare 2, seems to imply a sudden strong increase in the rate and efficiency of particle acceleration. This might occur as the unstable loop interacts with the overlying field, as seen in panel (c) of the cartoon. At this point, some electrons might be accelerated back towards the western footpoint that brightened in flare 2.

5. Discussion and conclusions

Three flares took place on 14 and 15 April 2002 in AR 9893/9901, and in this paper we have investigated how the third and largest of these events prduced HXR emission from an already dense coronal loop (Veronig & Brown 2004). The previous flaring activity in AR 9893/9901 may be in part responsible for the high loop density. This loop became visible in radio images before the onset of the HXR impulsive phase, suggesting the presence of high energy electrons in the loop before flare 3, evaporating plasma into the loop, as observed by EIT. This early observation of non thermal electrons in the loop may be due to initial reconnection between neighbouring loop systems allowing a small amount of fast particles to be accelerated and the creation of a dense loop by evaporation.

We propose that this loop becomes unstable to high beta disruption caused by the ballooning instability. This allows what is ostensibly a post flare loop to become unstable, creating turbulence, heating and fast particle acceleration.

The already rather high density in loop before the onset of the impulsive phase allows electrons to be stopped in the corona (Veronig & Brown 2004), causing efficient heating and conductive evaporation of chromospheric plasma, increasing the density and temperature further.

The complexity of this active region means it becomes necessary to consider the flaring loops as a dynamic 3-dimensional system, which due to high density already present in the loop becomes unstable and leads to more interaction with the overlying field, this in turn causes more flaring activity and particle acceleration.

Acknowledgements. L.B. acknowledges the support of a PPARC studentship and travel support from the University of Glasgow to attend the RHESSI fifth general workshop in Locarno, Switzerland. L.F. and J.C.B. acknowledge the support of a PPARC Rolling Grant. A.V. acknowledges the suppost of the Austrian Science Fund (FWF grant P15344) and research visitor funds from the Royal society of Edinburgh and from PPARC.

References

Brown, J. C., & McClymont, A. N. 1976, Sol. Phys., 49, 329
Dulk, G. A., & Dennis, B. R. 1982, ApJ, 260, 875
Ellison, D. C., & Ramaty, R. 1985, ApJ, 298, 400
Fletcher, L., & Martens, P. C. H. 1998, ApJ, 505, 418
Frost, K. J., & Dennis, B. R. 1971, ApJ, 165, 655
Hamilton, B., Fletcher, L., McClements, K. G., & Thyagaraja, A. 2005, ApJ, 625, 496

Hudson, H. S. 1978, ApJ, 224, 235
Kane, S. R., Anderson, K. A., Evans, W. D., Klebesadel, R. W., & Laros, J. 1979, ApJ, 233, L151
Kane, S. R., McTiernan, J. M., & Hurley, K. 2005, A&A, 433, 1133
Karlický, M., & Kosugi, T. 2004, A&A, 419, 1159
Kosugi, T., Sakao, T., Masuda, S., et al. 1994, in Proceedings of Kofu Symposium, 127
Krucker, S., Hurford, G. J., & Lin, R. P. 2003, ApJ, 595, L103
Lin, R. P., Schwartz, R. A., Pelling, R. M., & Hurley, K. C. 1981, ApJ, 251, L109
Lin, R. P., Krucker, S., Holman, G. D., et al. 2003, in Proceedings of the 28th international cosmic ray conference, 3207
Litvinenko, Y. E. 2003, Sol. Phys., 216, 189
Liu, W., Jiang, Y. W., Liu, S., & Petrosian, V. 2004, ApJ, 611, L53
Masuda, S., Kosugi, T., Hara, H., Tsuneta, S., & Ogawara, Y. 1994, Nature, 371, 495
Miller, J. A., Larosa, T. N., & Moore, R. L. 1996, ApJ, 461, 445
Park, W., Fredrickson, E. D., Janos, A., Manickam, J., & Tang, W. M. 1995, Phys. Rev. Lett., 75
Ramaty, R. 1969, ApJ, 158, 753
Ramaty, R., Schwartz, R. A., Enome, S., & Nakajima, H. 1994, ApJ, 436, 941
Shibasaki, K. 2001, ApJ, 557, 326
Somov, B. V., & Kosugi, T. 1997, ApJ, 485, 859
Sui, L. & Holman, G. D. 2003, ApJ, 596, L251
Sui, L., Holman, G. D., & Dennis, B. R. 2004, ApJ, 612, 546
Takakura, T., Tsuneta, S., Nitta, N., et al. 1983, ApJ, 270, L83
Takakura, T., Kundu, M. R., McConnell, D., & Ohki, K. 1985, ApJ, 298, 431
Tomczak, M. 2001, A&A, 366, 294
Tsuneta, S., & Naito, T. 1998, ApJ, 495, L67
van Beek, H. F., de Jager, C., Schadee, A., et al. 1981, ApJ, 244, L157
Veronig, A. M., & Brown, J. C. 2004, ApJ, 603, L117
Veronig, A. M., Karlický, M., Vršnak, B., et al. 2006, A&A, 446, 675
Wheatland, M. S., & Melrose, D. B. 1995, Sol. Phys., 158, 283